Supplementary Materials for

Metacavity Quantum Electrodynamics

Xueshi Li,[1,*] Ziwei Wang,[2,*] Yan Chen,[1,†] Dong Liu,[3] Kaili Xiong,[1] Guangfeng Wang,[2] Jiantao Ma,[3] Ying Yu,[3] Jiawei Wang,[4] Zhanling Wang,[5] Xiao Li,[6] Xianfeng Chen,[2,7,8] Erez Hasman,[9] Bo Wang,[2,‡] Jin Liu,[3,§] and Tian Jiang[1,10,¶]

[1]*College of Science, National University of Defense Technology, Changsha, 410073, China.*

[2]*State Key Laboratory of Photonics and Communications, School of Physics and Astronomy, Shanghai Jiao Tong University, Shanghai, 200240, China.*

[3]*State Key Laboratory of Optoelectronic Materials and Technologies, Sun Yat-sen University, Guangzhou, 510275, China.*

[4]*School of Integrated Circuits, Harbin Institute of Technology (Shenzhen), Shenzhen 518055, China.*

[5]*College of Electronic Science and Technology, National University of Defense Technology, Changsha, 410073, China.*

[6]*College of Advanced Interdisciplinary Studies, National University of Defense Technology, Changsha, 410073, China.*

[7]*Shanghai Research Center for Quantum Sciences, Shanghai, 201315, China.*

[8]*Collaborative Innovation Center of Light Manipulations and Applications, Shandong Normal University, Jinan, 250358, China.*

[9]*Atomic-Scale Photonics Laboratory, Russell Berrie Nanotechnology Institute, and Helen Diller Quantum Center, Technion Israel Institute of Technology, Haifa, 3200003, Israel.*

[10]*Hunan Research Center of the Basic Discipline for Physical States, Changsha, 410073, China.*

[*] These authors contribute equally to this research.

[†] chenyan@nudt.edu.cn; These authors contribute equally to this research.

[‡] wangbo89@sjtu.edu.cn

[§] liujin23@mail.sysu.edu.cn

[¶] tjiang@nudt.edu.cn

1. Theoretical analysis of the metacavity

1.1 Field analysis of the circular Bragg cavity

As a starting point, we analyze the field distribution in a circular Bragg cavity characterized by radial period P, ring half width R, cavity medium refractive index n_s, and surrounding air refractive index n_a (1). We only focus on the transverse electric (TE) mode, described by the out-of-plane magnetic field component H_z, which satisfies the Helmholtz equation:

$$\nabla^2 H_z + k^2(\boldsymbol{\rho}) H_z = 0 \qquad (S1)$$

Here, $\boldsymbol{\rho} = (r, \theta, z)$ denotes the position vector of a point in space. Owing to the rotational symmetry of the circular Bragg cavity, the Helmholtz equation for $H_z(r, \theta, z)$ is expressed in cylindrical coordinates:

$$\frac{\partial^2 H_z}{\partial r^2} + \frac{1}{r}\frac{\partial H_z}{\partial r} + \frac{1}{r^2}\frac{\partial^2 H_z}{\partial \theta^2} + \frac{\partial^2 H_z}{\partial z^2} + k^2(\boldsymbol{\rho}) H_z = 0$$

To solve the partial differential equation (PDE), we apply the method of separation of variables, treating r, θ, and z as independent functions:

$$H_z(r, \theta, z) = R(r)\Theta(\theta)e^{i\beta z}$$

Here, $R(r)$ and $\Theta(\theta)$ denote the radial and angular components, respectively. Neglecting the field variation along the z-direction, we set $\beta = 0$. So, we have:

$$\frac{r^2 R^{''} + rR^{'} + k^2(\boldsymbol{\rho}) r^2 R}{R} = -\frac{\Theta^{''}}{\Theta}$$

Since both sides of this PDE depend on independent variables, they must be equal to the same constant as m^2. Owing to the inherent 2π-periodicity of the angular coordinate θ, the solution for $\Theta(\theta)$ takes the form $\Theta(\theta) = Ce^{im\theta},\ m \in \mathcal{Z}$. For the radial component $R(r)$, we obtain a standard Bessel equation, whose general solution can be expressed as: $R(r) = AJ_m(k(\boldsymbol{\rho})r) + BY_m(k(\boldsymbol{\rho})r)$. Thus, we obtain expression for $H_z(r, \theta, z)$:

$$H_z(r, \theta, z) = [AJ_m(k(\boldsymbol{\rho})r) + BY_m(k(\boldsymbol{\rho})r)]e^{im\theta}, m \in \mathcal{Z}$$

Now we start to consider the spatially varying refractive index in the circular Bragg cavity, the local wave vector at different positions is given by $k(\boldsymbol{\rho}) = k_0 n(r)$, where $k_0 = \frac{2\pi}{\lambda}$ is wave vector in vacuum. The radial refractive index distribution $n(r)$ can be expressed as:

$$n(r) = \begin{cases} n_a, & r \in [NP - R, NP + R] \\ n_s, & elsewhere. \end{cases}$$

where N is a positive integer representing the N-th air layer. Equivalently, if both air and dielectric layers are indexed by j, the refractive index of j-th layer is:

$$n_j = \begin{cases} n_a, & j = even \\ n_s, & j = odd \end{cases} \qquad (S2)$$

where the even layer $j = 2N$ corresponds to the N-th air layer centered dt $r = NP$.
By defining $\gamma_j = k_0 n_j$ the field in each layer of the circular Bragg cavity can be written as:

$$\mathrm{H_z^j(r,\theta) = [A_j J_m(\gamma_j r) + B_j Y_m(\gamma_j r)] e^{im\theta}, m \in \mathcal{Z}} \qquad (S3)$$

1.2 Obtaining the cavity resonance wavelength from the Bragg condition

Next, we discuss the Bragg condition of the circle Bragg cavity. For an arrangement with a radial period P, multiple small reflections occur in the radial direction. The constructive interference of these reflections forms strong reflection bands, analogous to a one-dimensional distributed Bragg reflector (DBR). The approximate Bragg condition for the radial direction requires that the phase accumulated by the radial wave vector k between two neighboring layers satisfies the Bragg phase condition, i.e., the phase interference of consecutive reflected waves. The simplest approximate form is:

$$kP = q\pi, \qquad q = (1,2,3 \ldots)$$

Here, we defined $k = n_{eff} k_0$, where n_{eff} is the effective refractive index of the cavity, which can be determined from the radial refractive index profile $n(r)$. When the phase change of the light wave is π after propagating one cavity period P, the electric field experiences coherent cancellation, corresponding to the first-order Bragg condition ($q = 1$):

$$\lambda_1 = 2 n_{eff} P \qquad (S4)$$

Therefore, under first-order Bragg condition gives an approximate resonance wavelength λ_1 of the eigenproblem Eq.(S1).

1.3 Convert H_z into the in-plane circularly polarized electrical field component of $E_{\sigma+}$ and $E_{\sigma-}$

By using the relationship:

$$E_r = \frac{i}{\omega_0 \varepsilon} \frac{1}{r} \frac{\partial H_z}{\partial \theta} \;, \; E_\theta = -\frac{i}{\omega_0 \varepsilon} \frac{\partial H_z}{\partial r}$$

where $\omega_0 = ck_0$, $\varepsilon = \varepsilon_0 n^2$, we obtain the radial and angular components of in-plane electric field in the j-th layer of the circular Bragg cavity:

$$E_r^j(r,\theta) = -\frac{m}{ck_0 \varepsilon_0 n_j^2 r} [A_j J_m(\gamma_j r) + B_j Y_m(\gamma_j r)] e^{im\theta} \qquad (S5)$$

$$E_\theta^j(r,\theta) = -\frac{i}{c\varepsilon_0 n_j} \left[A_j J_m^{'}(\gamma_j r) + B_j Y_m^{'}(\gamma_j r) \right] e^{im\theta} \qquad (S6)$$

In the first layer, finiteness at $r \to 0$ requires $B_1 = 0$, and thus we can assume $A_1 = 1$. At the boundary of each layer, the fields satisfy the continuity condition:

$$H_z^j(r_{j,j+1}, \theta) = H_z^{j+1}(r_{j,j+1}, \theta), \; E_\theta^j(r_{j,j+1}, \theta) = E_\theta^{j+1}(r_{j,j+1}, \theta)$$

with $r_{j,j+1} = \begin{cases} \frac{j+1}{2}P - R, & j = odd \\ \frac{j}{2}P + R, & j = even \end{cases}$. Using this recursive relationship, the coefficients A_j and B_j for each layer can be determined.

Next, the field is converted to the circularly polarized form by using $E_{\sigma+} = e^{-i\theta}(E_r - iE_\theta)$ and $E_{\sigma-} = e^{i\theta}(E_r + iE_\theta)$:

$$E^j_{\sigma+}(r,\theta) = e^{i(m-1)\theta}\frac{-1}{c\varepsilon_0 n_j}\left[A_j J_{m-1}(\gamma_j r) + B_j Y_{m-1}(\gamma_j r)\right] = e^{i(m-1)\theta}D^j_{\sigma_+}(r) \quad (S7)$$

$$E^j_{\sigma-}(r,\theta) = e^{i(m+1)\theta}\frac{-1}{c\varepsilon_0 n_j}\left[A_j J_{m+1}(\gamma_j r) + B_j Y_{m+1}(\gamma_j r)\right] = e^{i(m+1)\theta}D^j_{\sigma_-}(r) \quad (S8)$$

1.4. Discretization the circular Bragg cavity into a GP metacavity

To manipulate the resonant modes of the circular Bragg cavity, each air layer (n_a with even index j) is discretized into a set of circular holes with C_8 symmetry arrangement, with $8N$ circular holes per layer, where $N = \frac{j}{2}$. We assume that the impact of this discretization on the distribution of mode's electric field is negligible. Therefore, the phase distribution of σ_+ and σ_- components can be expressed as:

$$Arg\left[E_{\sigma_+}(r)\right] = (m-1)\theta + Arg\left[D_{\sigma_+}(r)\right]$$

$$Arg\left[E_{\sigma_-}(r)\right] = (m+1)\theta + Arg\left[D_{\sigma_-}(r)\right]$$

Under the first-order Bragg condition Eq.(S4) and the relationship of A_j and B_j, $D_{\sigma_+}(r)$ and $D_{\sigma_-}(r)$ exhibit opposite signs within the same air layers (at $r = NP$), while they have the opposite signs relative to the adjacent layers i.e., $D_{\sigma_\pm}(r+P)$. The boundary between positive and negative values occurs approximately at $r = \frac{jP}{2}$ (with j being a positive odd number greater than 1), where the mode intensity approaches zero, indicating a singularity. Therefore, the cavity mode $|E_c\rangle$ at each air holes ($r = NP$) can be written in the terms of $|\sigma_+\rangle$ and $|\sigma_-\rangle$ as:

$$|E_c\rangle = e^{i(m-1)\theta}e^{\frac{i\pi r}{P}}\left|D_{\sigma_+}(r)\right||\sigma_+\rangle + e^{i(m+1)\theta}e^{\frac{i\pi(r+P)}{P}}\left|D_{\sigma_-}(r)\right||\sigma_-\rangle \qquad (S9)$$

Here, m is determined by the polarization state of the photon exciting the cavity ($m = +1$ for σ_+ and $m = -1$ for σ_-). The formulation clearly demonstrates the phenomenon of spin-orbit coupling (SOC) in $|E_c\rangle$. Specifically, when the cavity is excited by σ_+ photon ($m = +1$), the co-polarized component $|\sigma_+\rangle$ does not carry an angular phase term related to θ, whereas the cross-polarized component $|\sigma_-\rangle$ has a second-order orbit angular momentum (OAM).

Next, we perturb the circular holes into elliptical hole (neglecting the impact on the cavity modes) and apply a geometric phase rotation angle distribution $\theta_g(x,y)$, the modulated photon's state $|E_{ph}\rangle$ can be expressed as:

$$|E_{ph}\rangle = e^{-i2\theta_g}\langle\sigma_-|E_c\rangle|\sigma_+\rangle + e^{i2\theta_g}\langle\sigma_+|E_c\rangle|\sigma_-\rangle = \\ |D_{\sigma_-}(r)|e^{i\left[(m+1)\theta-2\theta_g+\frac{\pi(r+P)}{P}\right]}|\sigma_+\rangle + |D_{\sigma_+}(r)|e^{i\left[(m-1)\theta+2\theta_g+\frac{\pi r}{P}\right]}|\sigma_-\rangle \qquad (S10)$$

To achieve direction (Device I), spin-momentum-locked (Device II) and OAM (Device III) radiation as described in the main text, the meta-atoms configuration and the modulated photons state are designed as follows:

$$\theta_g = \frac{1}{2}\left(\frac{\pi r}{P} + 2\pi\boldsymbol{k_i}\cdot\boldsymbol{r} + n_i\theta\right) \qquad (S11)$$

$$|E_{ph}\rangle = |D_{\sigma_-}(r)|e^{i[(m+1-n_i)\theta-2\pi\boldsymbol{k_i}\cdot\boldsymbol{r}-\pi]}|\sigma_+\rangle \\ +|D_{\sigma_+}(r)|e^{i\left[(m-1+n_i)\theta+2\pi\boldsymbol{k_i}\cdot\boldsymbol{r}+\frac{2\pi r}{P}\right]}|\sigma_-\rangle, r = NP \qquad (S12)$$

Here $\mathbf{k_i} = (k_{ix}, k_{iy})$ represents the designed momentum in *k*-space, and n_i denotes the intended OAM number, $\mathbf{r} = (x,y)$ represents the real space location vector. The terms π and $\frac{2\pi r}{P}$ are uniform phase offsets and do not affect the modulation of the photons, where only the discrete values of $r = NP$ are obtained.

For Device I, we set $\mathbf{k_i} = (0,0), n_i = 0$. The GP configuration is $\theta_{g\mathrm{I}} = \frac{\pi r}{2P}$. So, we can get:

$$|E_{phI}\rangle = |C_{\sigma_-}(r)|e^{i(m+1)\theta}|\sigma_+\rangle + |C_{\sigma_+}(r)|e^{i(m-1)\theta}|\sigma_-\rangle$$

For Device II, we set $\mathbf{k_i} = (0.32,0), n_i = 0$. The GP configuration is $\theta_{g\mathrm{II}} = \frac{\pi r}{2P} + 0.32\pi x$. So, we can get:

$$|E_{phII}\rangle = |C_{\sigma_-}(r)|e^{i[(m+1)\theta-2\pi k_{ix}x]}|\sigma_+\rangle + |C_{\sigma_+}(r)|e^{i[(m-1)\theta+2\pi k_{ix}x]}|\sigma_-\rangle$$

For Device III, we set $\mathbf{k_i} = (0,0), n_i = 1$. The GP configuration is $\theta_{g\mathrm{III}} = \frac{\pi r}{2P} + \frac{\theta}{2}$. So, we can get:

$$|E_{phIII}\rangle = |C_{\sigma_-}(r)|e^{im\theta}|\sigma_+\rangle + |C_{\sigma_+}(r)|e^{im\theta}|\sigma_-\rangle$$

For Device IV, it can be understood as the superposition of multiple Device II functions to form a holographic pattern in *k*-space, the corresponding GP configuration is $\theta_{g\mathrm{IV}} = \frac{1}{2}\mathrm{Arg}(\sum_s e^{i[\frac{\pi r}{P}+2\pi\mathbf{k}_s\cdot\mathbf{r}]})$, $\mathbf{k}_s$ represents the designed hologram spot in *k*-space.

Taking Device III as an example, when quantum dots excite the metacavity with polarization states of both σ_+ and σ_-. $|E_{ph\mathrm{III}}\rangle$ manifests as both $|\sigma_+\rangle$ and $|\sigma_-\rangle$ components forming $\pm 1^{\mathrm{st}}$-order OAM as shown in Figure 4 of the main text.

2. Numerical Simulations

2.1 Robustness analysis of geometric parameters in the metacavity

we analyzed the robustness by combining experimental scanning electron microscope (SEM) characterizations — which indicate low spatial disorder in the fabricated devices — with a comprehensive parameter study of the key geometric parameters. In fact, high-Purcell-factor modes can be obtained over a range of parameter values, and the device performance evolves smoothly with parameter variations, indicating robust behavior of the proposed metacavity.

Parameters related to feature size, such as r (radius of meta-atoms, $r = D/2$) and R_c may experience systematic fabrication deviations during processing. Such variations can be effectively compensated through iterative optimization of the device layout during the design stage. Meanwhile, the overall device uniformity remains sufficiently high, as confirmed by SEM analysis of fabricated samples [**Fig. S1(a)**]. Statistical measurements and histogram of the elliptical holes show standard deviations σ of 2.41 nm and 1.82 nm for the major and minor axes, respectively, indicating good fabrication uniformity [**Fig. S1(b, c)**]. Therefore, random disorder effects have a negligible impact on device performance.

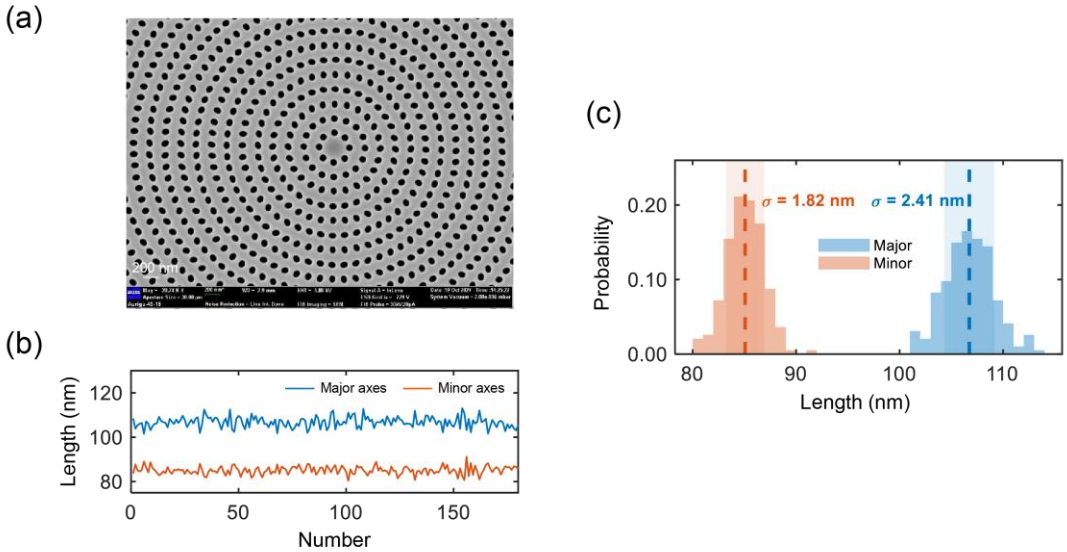

Figure S1: **SEM characterization and statistical uniformity of fabricated meta-atoms. (a)** SEM image of the fabricated metacavity structure; **(b)** Statistical variation and **(c)** histogram of the major and minor axes of the elliptical meta-atoms. Here, σ denotes the standard deviation.

2.2 Influence of key geometric parameters r, R_c, and anisotropy δ on metacavity performance

To further clarify the robustness of the device, we conducted the one-dimensional parameter sweeps of the radius r ($r = D/2$) of meta-atoms circular holes, the distance from the first circular hole to the center of the cavity R_c and anisotropy parameter δ, showing their influence on the resonance wavelength λ, Purcell factor F_p, and vertical radiation quality factor Q_V (**Fig. S2**), all the calculations were performed with radial periodicity P kept constant.

The Finite-Difference Time-Domain (FDTD) method was used for all numerical simulations. The simulation results show that r mainly affects the resonant wavelength [the black squares in **Fig. S2(a)**]: when r changes from 38 nm to 48 nm, the resonant wavelength decreases from 1000 nm to 900 nm. In contrast, R_c primarily affects F_p [the blue dots in **Fig. S2(b)**]: as R_c increases from 0.4 to 0.6, the Purcell factor rises dramatically from 10 to 400, while the resonant wavelength remains almost unchanged. However, when R_c exceeds 0.55, the area of near-field mode is very small, resulting in far-field radiation point with broad divergence angle. Such cavity modes are unsuitable for geometric phase manipulation.

We investigated the influence of anisotropy δ. As shown in **Fig. S2(c)**, δ has a minor influence on both λ and F_p. The quality factor Q of the cavity is determined by energy dissipation, where the total dissipation rate γ is the sum of the in-plane dissipation γ_H and the vertical radiation loss γ_V, expressed as $\gamma = \gamma_H + \gamma_V$. Consequently, the total quality factor satisfies the relation $\frac{1}{Q} = \frac{1}{Q_H} + \frac{1}{Q_V}$, where Q_H and Q_V represent the in-plane and vertical radiation quality factors, respectively. Specifically, Q_V characterizes the energy decay due to radiation into the free space from the thin film, while Q_H accounts for the lateral leakage into the surrounding meta-atom. When $\delta = 0$, all holes are circular and no vertical radiation channel exists, corresponding to $Q_V \rightarrow \infty$. in this case, the total quality factor reduces to the in-plane quality factor Q_H. As δ increases, the introduction of geometric phase progressively opens a vertical radiation channel, resulting in a decrease of Q while the resonant wavelength remains nearly unchanged. The dependence of Q on δ follows an approximately linear relation, which can be expressed as $Q = -k\delta + Q_H$. Thus, the corresponding expression for the vertical radiation quality factor can be derived as $Q_V = -Q_H + \frac{Q_H^2}{k}\delta^{-1}$, as shown in **Fig. S2(d)**.

All these data show that the device performance evolves smoothly with parameter variations, confirming that the proposed metacavity maintains stable operation under realistic fabrication tolerances. The parameters sweep ranges and their primary Impacted performances are shown in **Table S1.**

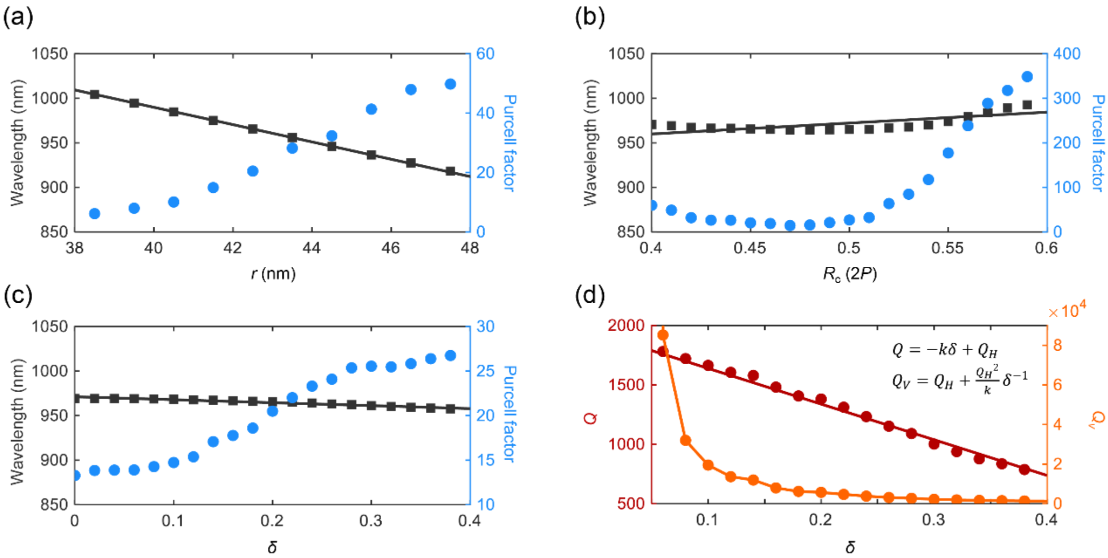

Figure S2: Influence of key parameters r, R_c, and δ on metacavity performance and robustness. (a) r primarily shifts the resonance wavelength λ, with a sensitivity of $d\lambda/dr \approx 10$ nm; **(b)** R_c significantly impacts F_p, which increases sharply to several hundred when $R_c > 0.55$; **(c)** δ has a minor effect on both λ and F_p while **(d)** predominantly governs the total quality factor Q and the vertical quality factor Q_V.

Table S1: Parameter Sweep Ranges and Impact

Varied Parameter	Sweep Range	Primary Impacted Performance	Resulting Range
r	38 − 48 nm	Resonance wavelength (λ)	1000 − 900nm
R_c	0.4 − 0.6 (2P)	Purcell Factor (F_p)	15 – 350 (non-monotonic)
δ	0 − 0.4	Vertical quality factor (Q_V)	$9\times10^4 - 2\times10^4$

Note: In all cases, the radial periodicity P and other parameters are kept constant.

We further investigated the influence of δ on effective mode volume V_{mode}. The V_{mode} decreases with δ [**Fig. S3(a)**]. Here, V_{mode} of the metacavity is defined as $V_{mode} = \frac{\int_{cavity} \varepsilon(\mathbf{r})|E(\mathbf{r})^2|dV}{\max\{\varepsilon(\mathbf{r})|E(\mathbf{r})^2|\}}$. We also examined the relationship between Purcell factor, resonant wavelength, Q and V_{mode}, that is $F_p \sim \frac{3}{4\pi^2}\left(\frac{\lambda}{n}\right)^3 (Q/V_{mode})$. The results show a good linear consistency of Purcell factor and $\lambda^3(Q/V_{mode})$ [**Fig. S3(b)**].

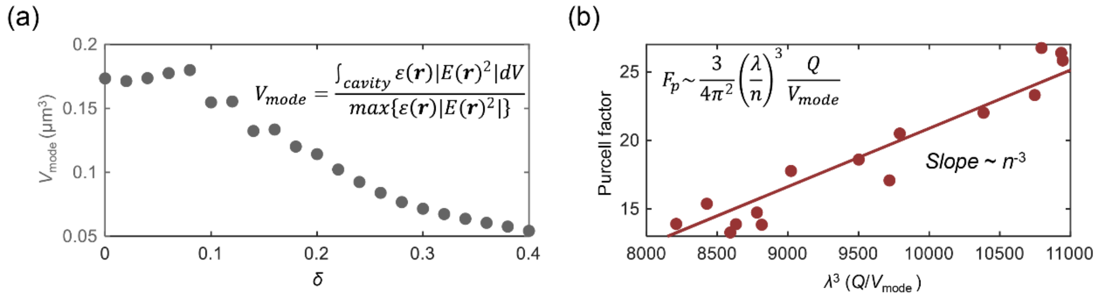

Figure S3: Effective mode volume V_{mode} and verification of the Purcell factor scaling relation. (a) Effective mode volume V_{mode}; **(b)** Examination of the consistency between Purcell factor and $\lambda^3(Q/V_{\mathrm{mode}})$, showing a good linear relationship.

2.3 Trade-off between near-field Purcell enhancement and wavefront control

We analyzed the full width at half maximum (FWHM) of the near-field (NF) and far-field (FF) electric field intensity distributions of resonant modes under different R_c [**Fig. S4(a)**]. The results show that as R_c varies, the FWHM of NF and FF modes exhibit opposite trends [**Fig.S4(b)**]. Numerical simulations show that, under optimized structural parameters, F_p can reach values on the order of several hundred, for example $F_p \sim 400$ at $R_c = 0.6$ [**Fig. S2(b)**].

However, our platform is designed not only to enhance spontaneous emission but also to enable wavefront engineering via geometric phase control. When the mode volume is further reduced, the near-field distribution becomes highly localized. Consequently, the emitted radiation exhibits large a divergence, this leads to a far-field full width at half maximum (FWHM) of approximately $0.25k_0$ [**Fig. S4(b)**], which is unfavorable for efficient geometric-phase-based wavefront control.

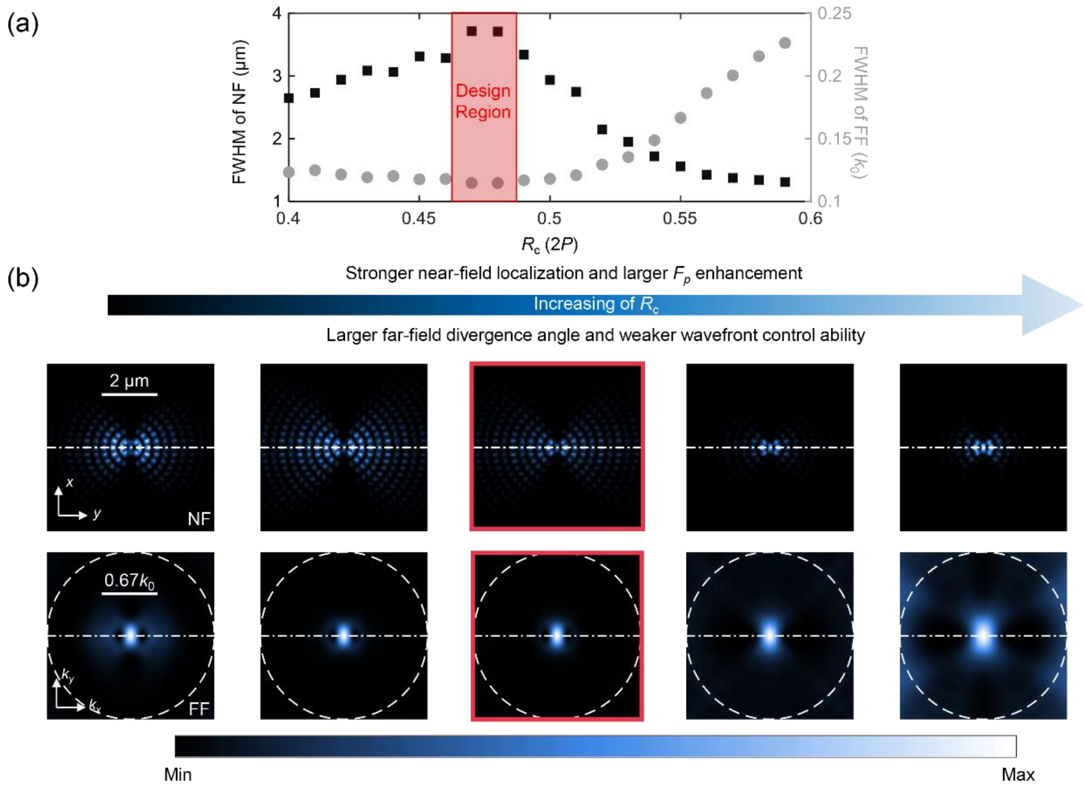

Figure S4: Impact of R_c on cavity mode characteristics. (a) Near-field and far-field FWHM; **(b)** Corresponding mode patterns. Red areas and boxes highlight our design parameters, balancing a moderate F_p with optimized near-field mode extension and low far-field divergence.

We have further performed simulations to verify that the mode volume V_{mode} indeed decreases as R_c increases within the range of 0.48 to 0.6, regardless of the perturbation (δ = 0 or 0.2) [**Fig. S5(a, b)**]. Simultaneously, the Q factor exhibits a "rise-and-fall" trend [**Fig. S5(c)**]. The synergy between Q and V_{mode} drives the variation of the Purcell factor observed in **Fig. S2(b)**. Furthermore, our calculations of the vertical radiation quality factor Q_V for $\delta = 0.2$ show that it remains nearly constant in the lower R_c regime and starts to increase sharply only when R_c exceeds 0.55 [**Fig. S5(d)**].

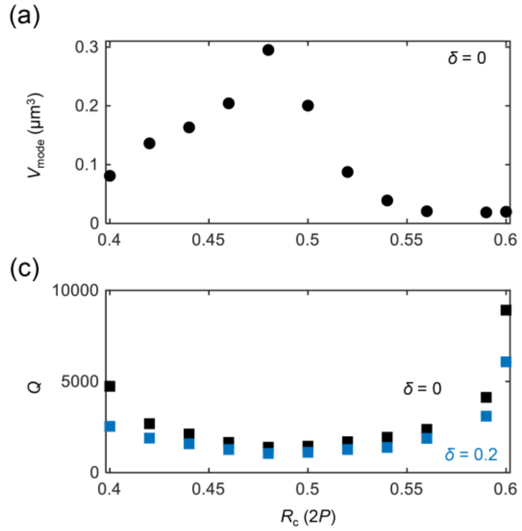

Figure S5: Theoretical analysis of cavity performance as a function of R_c. Calculated mode volume (V_{mode}) for the metacavity under **(a)** unperturbed ($\delta = 0$) and **(b)** perturbed ($\delta = 0.2$) conditions. **(c)** The quality factor Q versus R_c, exhibiting a "rise-and-fall" trend. **(d)** Vertical radiation quality factor Q_V ($\delta = 0.2$). All simulations were performed with the P and r kept constant.

2.4 Calculation for the radiation efficiency of the metacavity

A transmission box with a numerical aperture of ~0.9 was employed in simulation to calculate the radiation components (T_x, T_y, T_z) in different directions of the metacavity [**Fig. S6(a)**]. The total vertical radiation was obtained by summing the upward and downward T_z components, and the vertical radiation efficiency was defined as T_z / (T_x + T_y + T_z). The radiation components (T_x, T_y, T_z) and radiation efficiency with respect to r are shown in **Fig. S6(b)** and **Fig. S6(c)**, respectively. A higher vertical radiation efficiency (> 0.5) is observed when r exceeds 42 nm, which corresponds to the sizes used in our devices.

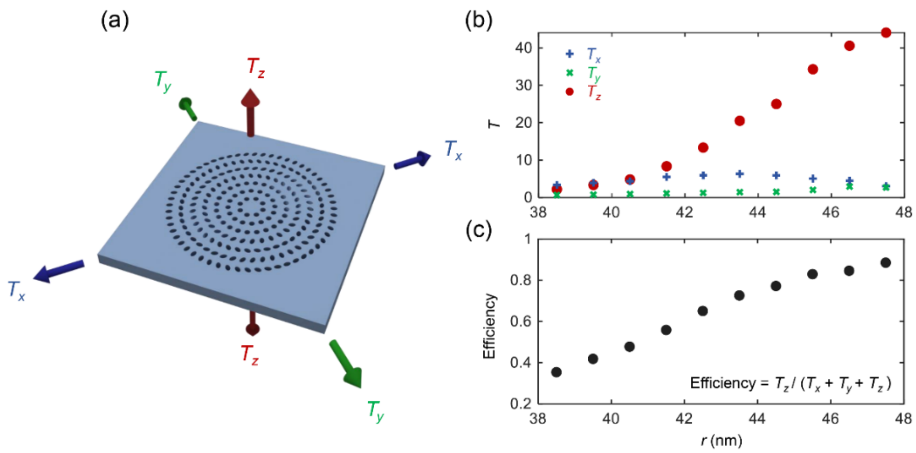

Figure S6: (a) Schematic diagram of metacavity radiation from transmission box. **(b)** Radiation components (T_x, T_y, T_z) in x, y and z directions and **(c)** vertical radiation efficiency of metacavity as a function of r.

2.5 Geometric phase verification in rotated meta-atom configuration

We verified the geometric phase induced by the rotation of meta-atoms on radiated photons. Based on the configuration of Device II [the gray dashed ellipses in **Fig. S7(a)**], a rotation angle of $\Delta\theta_g$ was applied to all meta-atoms in the cladding region, forming a new configuration [the red ellipses in **Fig. S7(a)**]. To examine the effect of this rotation, we calculated the phase $\varphi_{\sigma+}$ and $\varphi_{\sigma-}$ at the two radiation points ($k_{\sigma+}$,0) and ($k_{\sigma-}$,0) in the far-field [**Fig. S7(b)**]. The simulation results [**Fig. S7(c)**] show that the radiation photons of σ_+ and σ_- acquire opposite geometric phases, satisfying $\Delta\varphi_g = 2\sigma_\pm\Delta\theta_g$, where $\sigma_\pm$ denotes the spin of photons.

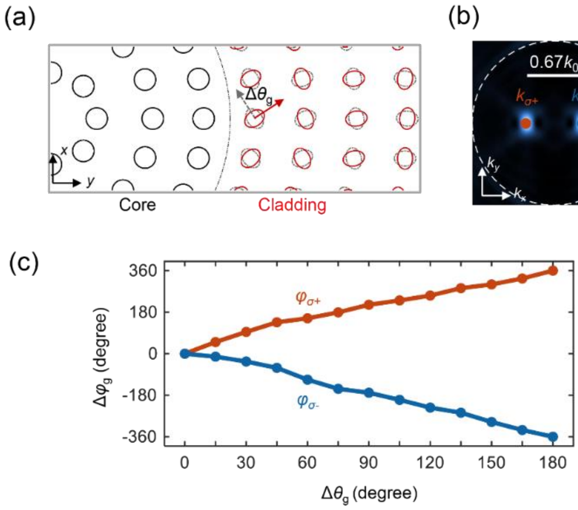

Figure S7: Verification of the geometric phase induced by meta-atom rotation. (a) For the metacavity of spin-momentum-locked configuration (device II), a rotation angle $\Delta\theta_g$ is applied to all meta-atoms in the cladding region. **(b)** Far-field radiation points at ($k_{\sigma+}$,0) and ($k_{\sigma-}$,0) are selected for phase analysis. **(c)** The corresponding points acquire opposite geometric phase $\Delta\varphi_g = 2\sigma_\pm\Delta\theta_g$, where $\sigma_\pm = \pm1$ denotes the spin of photons.

2.6 Metacavity designs for advanced light-field manipulations with Purcell enhancement

Furthermore, we demonstrated the capability of our cavity to achieve advanced manipulations of light field with high Purcell enhancement, beyond the three functions described in the main text. We designed a new meta-atoms configuration with a second-order OAM phase [**Fig. 8(b)**] using the same geometry phase design. This design produces a C_8-symmetric near-field mode with a Purcell factor of~40 at 945 nm [**Fig. S8(a)**] under circularly polarized σ_- excitation, thanks to the high symmetry of this designed configuration.

Due to the effect of spin–orbit coupling (SOC) and geometry phase, the cavity mode exhibits co-polarized component σ_- with $\ell = 0 - (-2) = +2$, and the cross-polarized component σ_+ with $\ell = 2 + (-2) = 0$ [**Fig. S8(c)**]. The distributions of electric field polarization vectors, intensity and phase of opposite-spin electric field along with the zoomed-in Stokes parameters ($|k| < 0.2k_0$) are also shown in **Fig. S8(c)**. The superposition of opposite-spin electric fields carrying 2nd and 0th order OAM respectively, signify the emergence of a three-dimensional vector light field, known as a skyrmion, a concept that has recently attracted significant attention. We further calculated the skyrmion number $N_{sk} = \frac{1}{4\pi}\iint \boldsymbol{S}\cdot\left(\frac{\partial S}{\partial x}\times\frac{\partial S}{\partial y}\right)dxdy = -2.001$, where the stokes vector $\boldsymbol{S} = (S_1, S_2, S_3)$ [**Fig. S8(d)**].

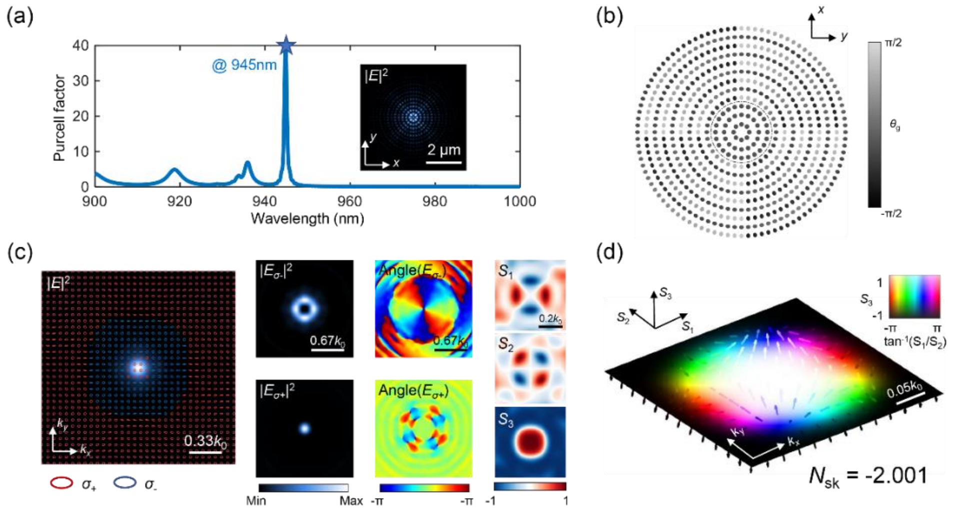

Figure S8: Generation of a skyrmion vector light field by second-order OAM phase configuration of metacavity. (a) Purcell factor and near-field mode of the metacavity with circularly polarized σ_- excitation, showing a Purcell factor of ~ 40 at 945 nm. **(b)** Meta-atoms configuration designed by second-order OAM phase configuration. **(c)** The distributions of electric field polarization vectors, intensity and phase of opposite-spin electric field along with the zoomed-in Stokes parameters ($|k| < 0.2k_0$). The co-polarized σ_- mode carries second-order OAM, while the cross-polarized σ_+ mode carries zeroth-order OAM. **(d)** Calculated skyrmion number N_{sk} from the Stokes vector $\boldsymbol{S} = (S_1, S_2, S_3)$.

Next, we designed configurations for third-order OAM phase and first-order OAM with spin-momentum-locked phase excited by σ_-. For the third-order OAM configuration, the cavity mode exhibits co-polarized component σ_- with $\ell = 0 - (-3) = +3$, and the cross-polarized component σ_+ with $\ell = 2 + (-3) = -1$ [**Fig. S9(a)**]; while for the first-order OAM with spin separation configuration, both the co-polarized and cross-polarized components exhibit $\ell = +1$, along with spin-momentum-locked [**Fig. S9(b)**].

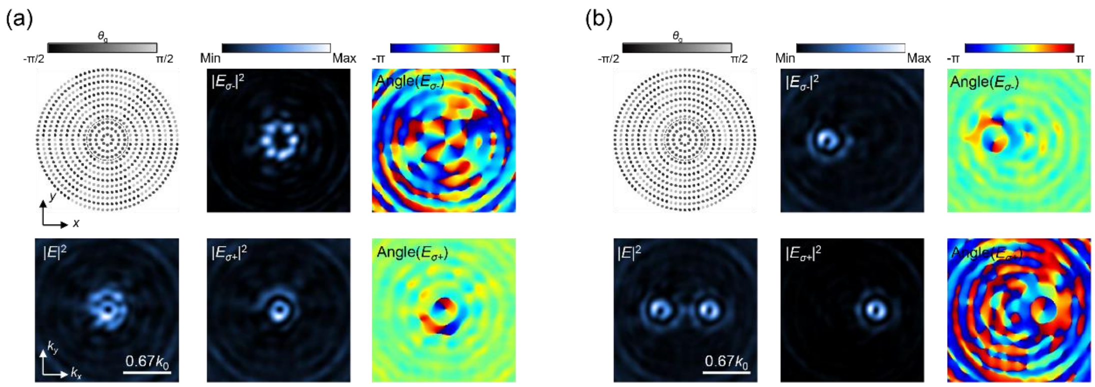

Figure S9: Metacavity design for higher-order OAM and first-order OAM with spin-momentum-locked excited by σ_-. (a) Third-order OAM phase configuration, resulting in co-polarized σ_- mode with $\ell = +3$, cross-polarized σ_+ mode with $\ell = -1$. **(b)** First-order OAM with spin-momentum-locked phase configuration, resulting in both co-polarized and cross-polarized modes carry $\ell = +1$ with opposite momentum separation.

3. Metacavity Fabrication

The device fabrication process is shown in **Fig. S10**. 40 pairs of bottom AlAs/GaAs distributed Bragg reflectors (DBR), a 600 nm $Al_{0.8}Ga_{0.2}As$ sacrificial layer, and a 200 nm GaAs layer with InAs QDs in the center are grown sequentially on a 350 μm-thick GaAs substrate via molecular beam epitaxy [**Fig. S10(a)**]. Subsequently, a 100 nm-thick SiN_x layer is deposited on the sample surface by chemical vapor deposition (CVD), and then a layer of photoresist is spin-coated [**Fig. S10(b)**]. The photoresist mask for the metacavity is fabricated by electron beam lithography (EBL) [**Fig. S10(c)**]. In the subsequent step, the metacavity pattern is transferred to the SiN_x layer via dry etching followed by oxygen plasma surface treatments [**Fig. S10(d)**]. In this process, SiN_x serves as a hard mask, enabling the realization of a highly selective etching effect. Next, the metacavity devices with QDs are fabricated by dry etching GaAs and removing the SiN_x layer [**Fig. S10(e)**]. Finally, the sample is dipped into a 2% hydrofluoric acid (HF) solution. After wet etching of the sacrificial layer with HF, the devices are transferred into deionized water, then into isopropanol (IPA). The IPA is then allowed to evaporate, leaving the devices suspended [**Fig. S10(f)**]. Devices are fabricated on the sample with medium-density QDs, where the QDs are randomly positioned. The fabricated suspended metacavity devices exhibit high structural quality, as confirmed by top-view [**Fig. S10(g)**] and cross-sectional [**Fig. S10(h)**] SEM imaging. Through systematic optimization of electron beam lithography (EBL) exposure parameters, dry etching conditions, and hard-mask lithography techniques, high-quality fabrication with vertical sidewalls and smooth surface morphology was achieved.

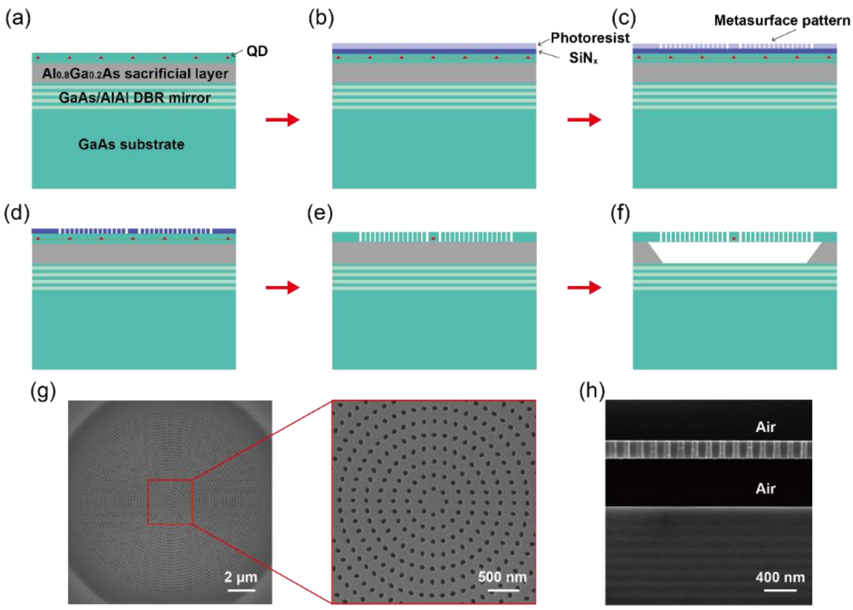

Figure S10: Fabrication process of metacavity devices. (a) Epitaxial growth of the bottom DBR, sacrificial layer, and QDs. **(b)** SiN_x deposition by CVD followed by photoresist spin-coating. **(c)** Fabrication of the photoresist mask by EBL. **(d)** Fabrication of the SiN_x mask by dry etching and photoresist stripping. **(e)** Fabrication of the metacavity with QDs by GaAs dry etching. **(f)** Removing the sacrificial layer by wet etching. **(g)** Top-view SEM images of a metacavity with a corresponding magnified region. **(h)** Cross-sectional SEM image of the metacavity.

4. Extraction efficiency of quantum dots (QDs) in the metacavity

To accurately calibrate the collection efficiency of single photons emitted from a quantum dot (QD) within the metacavity, we performed resonant excitation on device I and employed orthogonal polarization extinction to filter out the laser. The optical path is shown in **Fig. S11(a)**. The experimental far-field pattern of the single-photon emission from the QD in device I is shown in the inset, which exhibits a 98.75% similarity to a Gaussian mode (**Fig. S12**), enabling efficient coupling into an optical fiber for testing. The meta-cavities are fabricated on a 600-nm-thick sacrificial layer and a 40-period AlAs/GaAs DBR. The reflector is used to enhance the collection intensity of light in a reflection configuration and does not alter the resonant properties of the metacavity. The efficiency of each optical component in the path is shown in **Fig. S11(b)**, calibrated using a CW laser at the same wavelength as the QD emission. The overall system detection efficiency was determined to be 0.012. If alternative resonance schemes (such as two-color resonant excitation or phonon-assisted excitation) are adopted, along with the use of high-efficiency superconducting nanowire single-photon detector (SNSPD), a higher system detection efficiency can be achieved.

As shown in **Fig. S11(c)**, we measured an internal quantum efficiency (IQE) of 58% for the quantum dot within the metacavity. According to theoretical calculations, photons are completely localized within a first-order circular Bragg cavity. When perturbations are introduced, the mode symmetry is broken. Photons leak out in the vertical direction due to the geometric phase perturbations caused by the elliptical holes, resulting in a bright radiation spot at $|k_{\sigma\pm}\rangle = (0, 0)$. The internal quantum efficiency here represents the probability that an exciton recombination event yields a photon. Under resonant π-pulse excitation at 80 MHz, experimental data fitting [with the Rabi oscillation fitting referenced to (2)] reveals coherent population control with a preparation fidelity of 64% [**Figure S11(d)**] and a photon count rate of 176,000 counts per second [**Fig. S11(e)**]. By accounting for the system's total detection efficiency (0.012), the quantum dot internal quantum efficiency (0.58), the preparation fidelity (0.64) and the single-photon purity (0.983), we derived a single-photon extraction efficiency of 176k * 0.983 / 0.012 / 0.58 / 0.64 / 80M = 48.5%, i.e., the first-lens extraction efficiency.

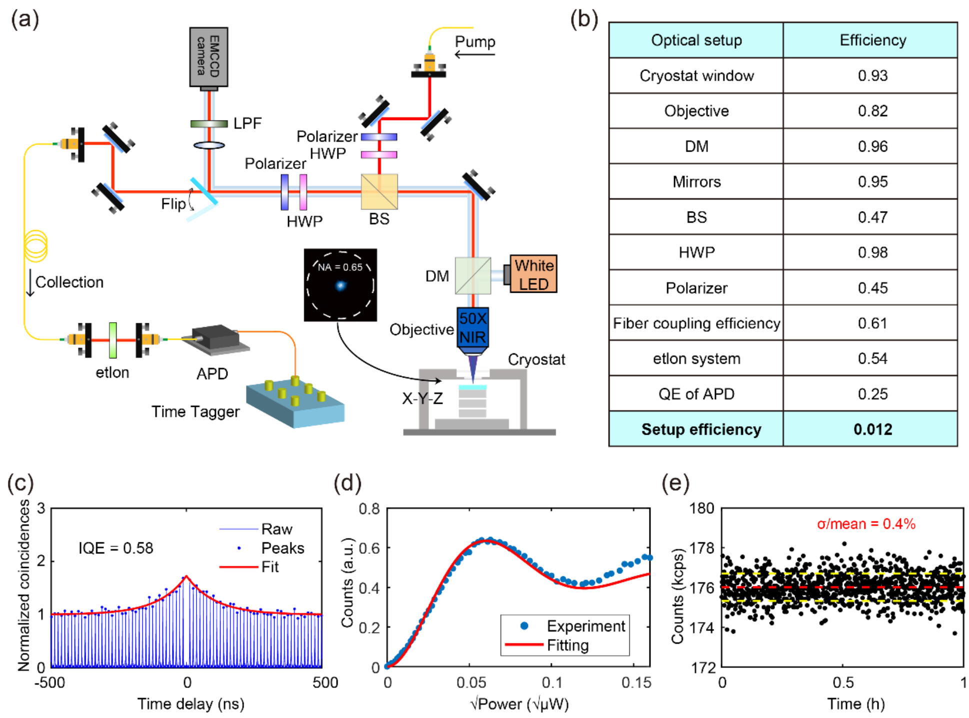

Optical setup	Efficiency
Cryostat window	0.93
Objective	0.82
DM	0.96
Mirrors	0.95
BS	0.47
HWP	0.98
Polarizer	0.45
Fiber coupling efficiency	0.61
etlon system	0.54
QE of APD	0.25
Setup efficiency	**0.012**

Figure S11: Setup efficiency calibration. (a) All the optical elements used in the collection path under 80 MHz pulsed resonant excitation conditions. Inset: *K*-space distribution from device I with quantum dots. **(b)** Transmissions of the optical elements in the setup with a total efficiency of 0.012. **(c)** The quantum dot internal quantum efficiency. **(d)** Rabi oscillations of Device I under resonant excitation. **(e)** Single-photon flux versus time of quantum dots in metacavity device.

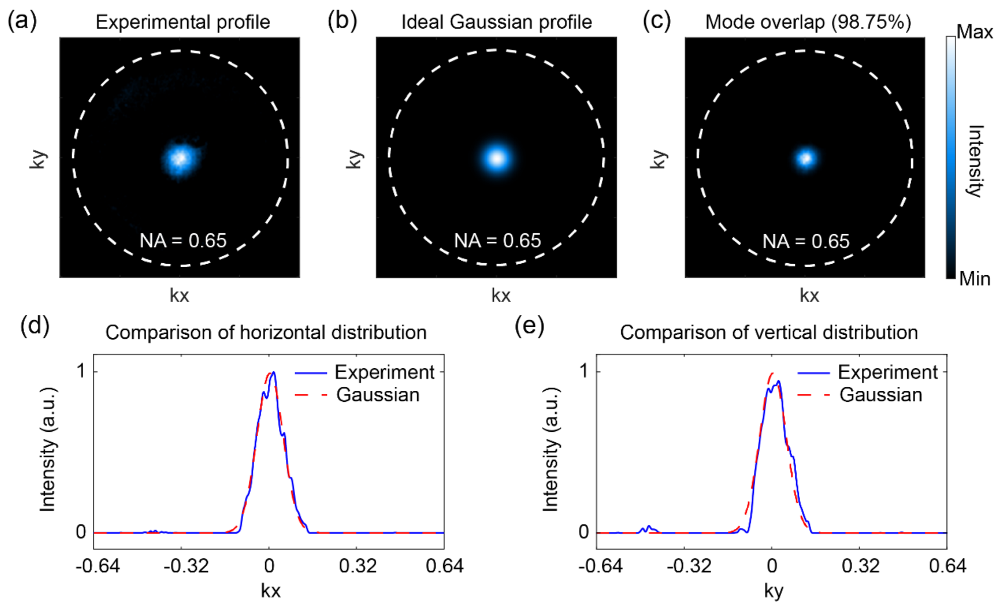

Figure S12: Overlap Analysis between the Experimental Far-Field Pattern and the Ideal Gaussian Mode.

5. Optical measurement system for the metacavity

The metacavity devices are located in a closed-cycle cryostat with a base temperature of 4.8 K. The QDs embedded in the metacavity can be excited by continuous wave (CW) or pulsed lasers via a ×50 objective with a numerical aperture of 0.65. The emitted single photons are collected by the same objective and sent to a spectrometer for spectral analysis or to avalanche photodiodes (APDs) for lifetime characterizations, Hanbury-Brown-Twiss (HBT) measurements, and Hong-Ou-Mandel (HOM) interference. A white light-emitting diode (LED) coupled to the main optical path with a 650 nm long-pass dichroic mirror (DM) and a beam splitter (BS) is used to illuminate the devices. To characterize the multi-dimensional quantum emissions engineered by meta-cavities, a Fourier-transform lens is flipped into the optical path and maps the far-field plane to an Electron-Multiplying Charge-Coupled Device (EMCCD). In the setup, a 4f system is implemented by inserting the additional lens between the objective and the imaging lens, which projects the back focal plane of the objective onto the EMCCD. This configuration directly maps the *k*-space (angular) distribution of the emitted photons. The single photons are spectrally filtered using a 900 nm long-pass filter (LPF) and a band-pass filter (BPF), followed by polarization verification with a quarter-waveplate (QWP) and polarizer. For the polarization-resolved measurements shown in **Fig. 4(d)** of the main text, a QWP and a linear polarizer are placed before the EMCCD. By rotating the QWP and polarizer, the left and right circular polarizations are distinguished. The corresponding spectra measured under these polarization conditions are shown in **Fig. S14**.

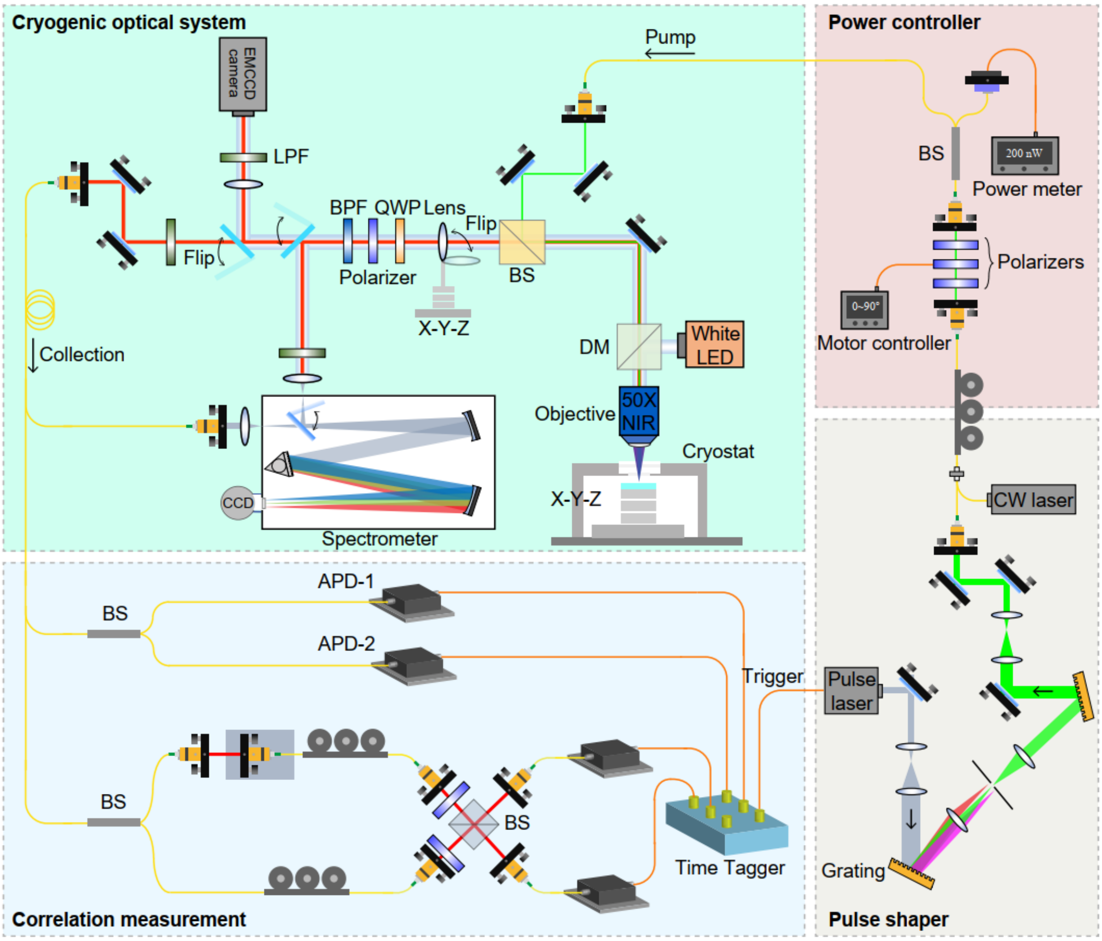

Figure S13: Schematic of the setup for optical characterizations.

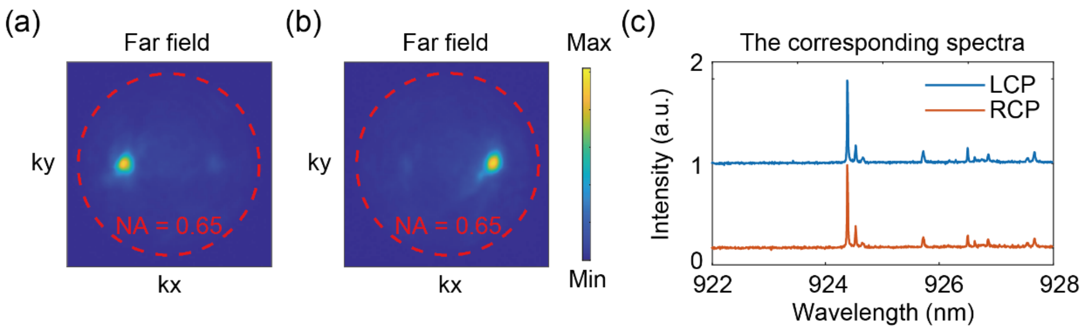

Figure S14: Polarization-resolved measurements of the emission from Device II. (a) Left circularly polarized (LCP) emission, **(b)** right circularly polarized (RCP) emission, and **(c)** the corresponding spectra.

6. Calibration of Hong-Ou-Mandel (HOM) interference

The two-photon interference visibility is quantified by the expression $1 - A_{/\!/} / A_{\perp}$, where $A_{\parallel}$ and $A_{\perp}$ represent the areas of the central peak in parallel and perpendicular polarized interference patterns, respectively. In our experimental setup, three main factors contribute to the reduction of the ideal interference visibility: (a) a non-zero $g^{(2)}(0)$ value, (b) imperfect classical interference visibility (1-ε), and (c) an unbalanced beam splitter with a reflectance-to-transmittance ratio of R:T = 46:54.

The central peak area can be expressed as (3):

$$A = N\eta\{(R^3T\ +\ T^3R)[1\ +\ 2g^2(0)]\ -\ 2(1-\varepsilon)^2R^2T^2V\} \qquad (S13)$$

N is the photon generation rate, η represents the combined efficiency of photon generation and detection, and V denotes the intrinsic interference visibility (V = 0 for distinguishable photons, V = 1 for perfect indistinguishability). From this relationship, we derive the corrected visibility formula (4) :

$$V_{cor} =\ [1/(1-\varepsilon)^2](R^2+T^2)/(2RT)(1\ +\ 2g^2(0))V_{raw} \qquad (S14)$$

Using our experimental parameters with 1 - $\varepsilon \approx$ 0.94 and incorporating all other relevant values into this equation, we obtain a corrected visibility of 0.865 after accounting for all these effects.

7. Metacavity tuning via parameter sweep (experiments)

In our experiments, we fabricated devices with different dimensions and characterized the cavity mode properties—including the resonant wavelength and quality factor (*Q*-factor)—as functions of various structural parameters, particularly the size of the circular holes. The devices were mainly divided into three categories: [**Fig. S15(a)**] a cavity consisting of circular holes with a period satisfying the second-order Bragg condition, [**Fig. S15(b)**] a cavity consisting of circular holes with a period meeting the first-order Bragg condition, and [**Fig. S15(c)**] a metacavity composed of both circular and elliptical holes with a period also satisfying the first-order Bragg condition. The spectra shown in Fig. S14 are cavity mode spectra, measured under high-power excitation of multiple QDs in the cavity.

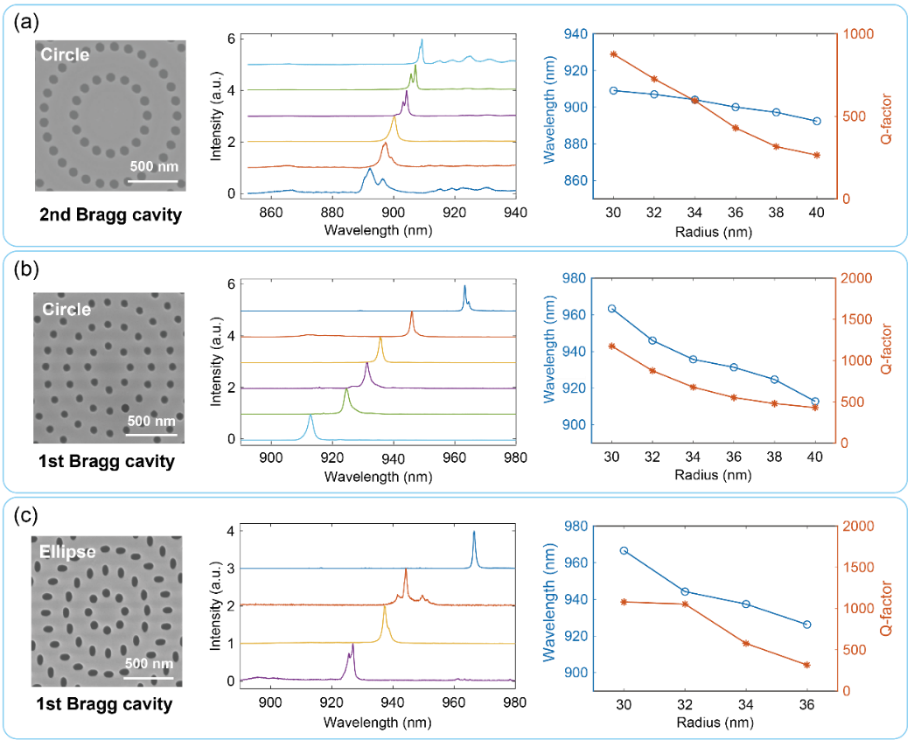

Figure S15: Cavity mode evolution under parameter sweeps of different cavity structures. (a) 2nd-order Bragg cavity (circle holes), **(b)** 1st-order Bragg cavity (circle holes), and **(c)** 1st-order Bragg cavity (circle + ellipse holes) showing SEM images, cavity mode, and *Q*-factor dependence on meta-atom dimensions.

References

1. J. Scheuer, A. Yariv, Annular Bragg defect mode resonators. *J. Opt. Soc. Am. B* **20**, 2285–2291 (2003).
2. P. Michler, Ed., Quantum Dots for Quantum Information Technologies *(Springer, New York,* 2017*);*
3. C. Santori, D. Fattal, J. Vučković, G. S. Solomon, Y. Yamamoto, Indistinguishable photons from a single-photon device. *Nature* **419**, 594–597 (2002).
4. J. Yang, Y. Chen, Z. Rao, Z. Zheng, C. Song, Y. Chen, K. Xiong, P. Chen, C. Zhang, W. Wu, Y. Yu, S. Yu, Tunable quantum dots in monolithic Fabry-Perot microcavities for high-performance single-photon sources. *Light Sci. Appl.* **13**, 33 (2024).